High-order ALE gas-kinetic scheme with WENO reconstruction

Liang Pan [a,*], Fengxiang Zhao [b], Kun Xu [c,b,d]

[a] *School of Mathematical Sciences, Beijing Normal University, Beijing, China*
[b] *Department of Mechanical and Aerospace Engineering, Hong Kong University of Science and Technology, Kowloon, Hong Kong*
[c] *Department of mathematics, Hong Kong University of Science and Technology, Kowloon, Hong Kong*
[d] *Shenzhen Research Institute, Hong Kong University of Science and Technology, Shenzhen, China*

ARTICLE INFO

ABSTRACT

In this paper, a high-order multi-dimensional gas-kinetic scheme is presented for both inviscid and viscous flows in arbitrary Lagrangian-Eulerian (ALE) formulation. Compared with the traditional ALE method, the flow variables are updated in the finite volume framework, and the rezoning and remapping steps are not required. The two-stage fourth-order method is used for the temporal discretization, and the second-order gas-kinetic solver is applied for the flux evaluation. In the two-stage method, the spatial reconstruction is performed at the initial and intermediate stages, and the computational meshes are determined by the mesh velocity. In the moving mesh procedure, the mesh may distort severely and the mesh quality is reduced. To achieve the accuracy and improve the robustness, the newly developed WENO method [40] on quadrilateral meshes is adopted at each stage. The Gaussian quadrature is used for flux calculation. For each Gaussian point, the WENO reconstruction is performed in local moving coordinate, where the variation of mesh velocity along cell interface is taken into account. Numerical examples are presented to validate the performance of current scheme, where the mesh adaptation method and the cell centered Lagrangian method are used to provide mesh velocities.

1. Introduction

In the computational fluid dynamics, there exist two coordinate systems to describe flow motions, where the Eulerian system describes flow motions with time-independent mesh and the mesh moves with the fluid velocity in the Lagrangian system. Considerable progress has been made over the past decades for the numerical simulations based on these two descriptions [3,24,36]. The Eulerian system is relatively simple, but it smears contact discontinuities and slip lines badly. For the computation with fixed boundaries, the Eulerian system could work effectively. However, in the problems with moving boundaries and bodies, it becomes difficult for the Eulerian method. On the other hand, the Lagrangian system could resolve contact discontinuities sharply, but the computation can easily break down due to mesh deformation. In order to avoid mesh distortion and tangling in the Lagrangian method, a widely used arbitrary-Lagrangian-Eulerian (ALE) technique was developed [14]. Generally, there are two types of ALE method, i.e. the direct method and indirect ALE method. The indirect ALE method contains three main stages, i.e. Lagrangian stage, rezoning stage and remapping stage. In the Lagrangian stage, the solution and the computational mesh are updated simultaneously. To release the error due to mesh deformation, the computational mesh is adjusted to the optimal position in the rezoning stage. In the remapping stage, the Lagrangian

---

solution is transferred into the rezoned mesh. For indirect ALE method, because it is based on a pure Lagrangian phase, the curvilinear grids have to be used to achieve very high-order accuracy. Further developments and great achievements have been made for the ALE method [1,20,10,37].

In the past decades, the gas-kinetic scheme (GKS) based on the Bhatnagar-Gross-Krook (BGK) model [4,6] has been developed systematically for computations from low speed flow to supersonic one [38,39]. Different from the numerical methods based on the Riemann flux [36], GKS presents a gas evolution process from kinetic scale to hydrodynamic scale, where both inviscid and viscous fluxes are recovered from a time-dependent and multi-dimensional gas distribution function at a cell interface. Recently, based on the time-dependent flux function, a two-stage fourth-order method was developed for Lax-Wendroff type flow solvers, particularly applied for the hyperbolic conservation laws [23,9,27–29]. Under the multi-stage multi-derivative framework, a reliable two-stage fourth-order GKS has been developed, and even higher-order of accuracy can be achieved. More importantly, this scheme is as robust as the second-order scheme and works perfectly from subsonic to hypersonic flows. Based on the unified coordinate transformation [12], the second-order gas-kinetic scheme was developed under the moving-mesh framework [15,16]. With the integral form of the fluid dynamic equations, a second-order remapping-free ALE gas-kinetic scheme was developed [26], in which the rezoning and remapping stages in the indirect ALE method are avoided. It can be considered as a direct ALE method, in which the grid velocity can be chosen arbitrarily in the flux calculation. For the indirect ALE method, the Lagrangian part has to be compatible with the geometric conservation law. However, for the direct ALE method, all those considerations vanish, as the grid displacement does not have to be physically related to problem under consideration. For the second-order scheme, a piecewise constant mesh velocity at each cell interface is considered. For the higher-order schemes, the variation of the mesh velocity along cell interface needs to be taken into account. Otherwise, the geometric conservation law may be violated during the mesh rotating and deformation. Recently, a one-stage DG-ALE gas-kinetic method was developed, especially for the oscillating airfoil calculations [32]. The variation of mesh velocity is considered in the time dependent flux calculation along a cell interface, and the geometric conservation law can be satisfied accurately. However, the one-stage gas evolution model and DG framework become very complicated, and the efficiency of the DG-ALE-GKS becomes low due to the severely constrained time step from the DG formulation.

In this paper, with the arbitrary Lagrangian-Eulerian (ALE) formulation, a high-order moving-mesh gas-kinetic scheme is developed for the inviscid and viscous flows, and it extends the gas-kinetic scheme from the static domain to the variable one. Compared with the traditional ALE method, the flow variables are updated in the finite volume framework, and the rezoning and remapping steps are not required. To deal with the distorted mesh generated in the moving-mesh process, a third-order WENO scheme [40] is used, in which the optimization approach for linear weights and the non-linear weights with new smooth indicator improves the robustness of WENO scheme. The two-stage fourth-order method is used for the temporal discretization. The computational meshes at the initial and intermediate stages are given by the mesh velocity, and the WENO reconstruction is performed at the initial and intermediate stage respectively. The mesh velocity inside each cell interface are considered and the WENO reconstruction is performed at each Gaussian quadrature point in the local moving coordinate. Thus, the accuracy and geometric conservation law can be well preserved by the current scheme even with the largely deforming mesh. Numerical examples are presented to validate the performance of current scheme, where the mesh adaptation method and the cell centered Lagrangian method are used to provide the mesh velocity.

This paper is organized as follows. In Section 2, the gas-kinetic scheme on moving-mesh is introduced. The extension of the two-stage temporal discretization to moving mesh system is presented in Section 3. In Section 4, we give the WENO reconstruction on unstructured quadrilateral meshes. Section 5 includes numerical examples to validate the current algorithm. The last section is the conclusion.

2. Gas-kinetic scheme on moving-meshes

The two-dimensional BGK equation can be written as [4,6],

$$f_t + u f_x + v f_y = \frac{g - f}{\tau}, \tag{1}$$

where f is the gas distribution function, g is the corresponding equilibrium state, and τ is the collision time. The collision term satisfies the compatibility condition

$$\int \frac{g - f}{\tau} \psi \, d\Xi = 0, \tag{2}$$

where $\psi = (1, u, v, \frac{1}{2}(u^2 + v^2 + \xi^2))$, $d\Xi = du dv d\xi^1 ... d\xi^K$, K is the number of internal degrees of freedom, i.e. $K = (4 - 2\gamma)/(\gamma - 1)$ for two-dimensional flows, and γ is the specific heat ratio. In the continuum regime, the gas distribution function can be expanded as

$$f = g - \tau D_{\boldsymbol{u}} g + \tau D_{\boldsymbol{u}}(\tau D_{\boldsymbol{u}})g - \tau D_{\boldsymbol{u}}[\tau D_{\boldsymbol{u}}(\tau D_{\boldsymbol{u}})g] + ...,$$

where $D_{\boldsymbol{u}} = \partial/\partial t + \boldsymbol{u} \cdot \nabla$. With the zeroth order truncation, i.e. $f = g$, the Euler equations can be obtained. For the Navier-Stokes equations, the first order truncation is used
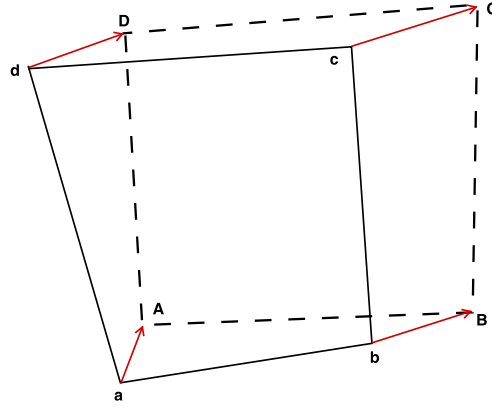
Fig. 1. Schematic for moving control volume: $\Omega(t)$ moves from $[abcd]$ at t^n to $[ABCD]$ at t^{n+1}.

$$f = g - \tau(u g_x + v g_y + g_t).$$

With the higher order truncations, the Burnett and super-Burnett equations can be obtained [38,39].

In this paper, the high-order ALE gas-kinetic scheme will be constructed in the moving-mesh framework. As shown in Fig. 1, a quadrilateral cell $\Omega(t)$ moves from $[abcd]$ at t^n to $[ABCD]$ at t^{n+1} with grid velocity $\boldsymbol{U}^g = (U^g, V^g)$, which varies along each segment. The boundary is given by

$$\partial\Omega_i(t) = \bigcup_m \Gamma_{im}(t),$$

where $\Gamma_{im}(t)$ is the line segment of boundary. For simplicity, the mesh velocity is set to be constant during a time interval, and the segments keep straight during a time step. Standing on the moving reference, the BGK equation Eq. (1) becomes

$$f_t + (u - U^g) f_x + (v - V^g) f_y = \frac{g - f}{\tau}. \tag{3}$$

Taking moments of the kinetic equation Eq. (3) and integrating with respect to space, the finite volume scheme can be expressed as

$$\frac{\mathrm{d}(|\Omega_i| W_i)}{\mathrm{d}t} = -\sum_m F_{im}(t), \tag{4}$$

where W_i is the cell averaged conservative value over Ω_i, $|\Omega_i|$ is the area of Ω_i and $F_{im}(t)$ is the time dependent fluxes across cell interface Γ_{im}, which is a line integral over Γ_{im}

$$F_{im}(t) = \int_{\Gamma_{im}} \left(\int \psi f(\boldsymbol{x}(s), t, \boldsymbol{u}, \xi)(\boldsymbol{u} - \boldsymbol{U}^g) \cdot \boldsymbol{n}_{im} \mathrm{d}\Xi \right) \mathrm{d}s,$$

where $f(\boldsymbol{x}(s), t, \boldsymbol{u}, \xi)$ is the gas distribution function in the global coordinate and $\boldsymbol{n}_{im} = (L_{im}, M_{im})$ is the outer normal direction of Γ_{im}. To simplify calculation and achieve high-order spatial accuracy, Gaussian quadrature is used for flux calculation

$$F_{im}(t) = |\Gamma_{im}| \sum_{p=1}^{2} \omega_{i,m_p} F_{i,m_p}(t),$$

where $\boldsymbol{x}_{i,m_p}$ is Gaussian quadrature point of the segment Γ_{im}, ω_{i,m_p} is the quadrature weight and $\boldsymbol{U}^g_{i,m_p}$ is the grid velocity of quadrature point. The numerical flux at $\boldsymbol{x}_{i,m_p}$ is defined as

$$F_{i,m_p}(t) = \begin{pmatrix} F^\rho_{i,m_p} \\ F^m_{i,m_p} \\ F^n_{i,m_p} \\ F^E_{i,m_p} \end{pmatrix} = \int \psi f(\boldsymbol{x}_{i,m_p}, t, \boldsymbol{u}, \xi)(\boldsymbol{u} - \boldsymbol{U}^g_{i,m_p}) \cdot \boldsymbol{n}_{im} \mathrm{d}\Xi.$$

In the formulation above, the grid velocity varies along a cell interface. Therefore, the translation, rotation and deformation are taken into account. With identified normal direction, the relative particle velocity at Gaussian point in the local coordinate is defined as

$$\begin{cases} \widetilde{u} = (u - U^g_{i,m_p})L_{im} + (v - V^g_{i,m_p})M_{im}, \\ \widetilde{v} = -(u - U^g_{i,m_p})M_{im} + (v - V^g_{i,m_p})L_{im}. \end{cases} \tag{5}$$

In the actual computation, the spatial reconstruction, which will be presented in the later section, is performed in a local moving coordinate. With the reconstructed variables, the gas distribution function is obtained at Gaussian quadrature point. The numerical flux can be obtained by taking moments of it, and the component-wise form can be written as

$$\widetilde{F}_{i,m_p}(t) = \begin{pmatrix} F^{\widetilde{\rho}}_{i,m_p} \\ F^{\widetilde{\rho U}}_{i,m_p} \\ F^{\widetilde{\rho V}}_{i,m_p} \\ F^{\widetilde{\rho E}}_{i,m_p} \end{pmatrix} = \int \widetilde{u} \begin{pmatrix} 1 \\ \widetilde{u} \\ \widetilde{v} \\ \frac{1}{2}(\widetilde{u}^2 + \widetilde{v}^2 + \xi^2) \end{pmatrix} f(\boldsymbol{x}_{i,m_p}, t, \widetilde{\boldsymbol{u}}, \xi) d\widetilde{\Xi},$$

where $f(\boldsymbol{x}_{i,m_p}, t, \widetilde{\boldsymbol{u}}, \xi)$ is the gas distribution function in the local coordinate. According to Eq. (5), the fluxes in the inertia frame of reference can be obtained as a combination of the fluxes in the moving frame of reference

$$\begin{cases} F^{\rho}_{i,m_p} = F^{\widetilde{\rho}}_{i,m_p}, \\ F^{\rho U}_{i,m_p} = (U^g_{i,m_p}F^{\widetilde{\rho}}_{i,m_p} + L_{im}F^{\widetilde{\rho U}}_{i,m_p} - M_{im}F^{\widetilde{\rho V}}_{i,m_p}), \\ F^{\rho V}_{i,m_p} = (V^g_{i,m_p}F^{\widetilde{\rho}}_{i,m_p} + M_{im}F^{\widetilde{\rho U}}_{i,m_p} + L_{im}F^{\widetilde{\rho V}}_{i,m_p}), \\ F^{\rho E}_{i,m_p} = (F^{\widetilde{\rho E}}_{i,m_p} + \frac{1}{2}((U^g_{i,m_p})^2 + (V^g_{i,m_p})^2)F^{\widetilde{\rho}}_{i,m_p} \\ \qquad\qquad + (L_{im}U^g_{i,m_p} + M_{im}V^g_{i,m_p})F^{\widetilde{\rho U}}_{i,m_p} + (-M_{im}U^g_{i,m_p} + L_{im}V^g_{i,m_p})F^{\widetilde{\rho V}}_{i,m_p}). \end{cases} \tag{6}$$

To construct the gas distribution function in the local coordinate, the integral solution of the BGK equation is used

$$f(\boldsymbol{x}_{i,m_p}, t, \boldsymbol{u}, \xi) = \frac{1}{\tau}\int_0^t g(x', y', t', u, v, \xi)e^{-(t-t')/\tau}dt' + e^{-t/\tau}f_0(-ut, -vt, u, v, \xi), \tag{7}$$

where $\widetilde{\boldsymbol{u}}$ is simply denoted as $\boldsymbol{u}$, $\boldsymbol{x}_{i,m_p} = (x_{i,m_p}, y_{i,m_p})$ is the location of Gaussian quadrature point, $\boldsymbol{x}_{i,m_p} = \boldsymbol{x}' + \boldsymbol{u}(t - t')$ is the trajectory of particle, f_0 is the initial gas distribution function, and g is the corresponding equilibrium state. According to the integral solution Eq. (7), $f(\boldsymbol{x}_{i,m_p}, t, \boldsymbol{u}, \xi)$ at the cell interface can be expressed as [39,38]

$$\begin{aligned} f(\boldsymbol{x}_{i,m_p}, t, \boldsymbol{u}, \xi) = &(1 - e^{-t/\tau})g_0 + ((t+\tau)e^{-t/\tau} - \tau)(\overline{a}_1 u + \overline{a}_2 v)g_0 \\ &+ (t - \tau + \tau e^{-t/\tau})\overline{A}g_0 \\ &+ e^{-t/\tau}g_r[1 - (\tau + t)(a_{1r}u + a_{2r}v) - \tau A_r)]H(u) \\ &+ e^{-t/\tau}g_l[1 - (\tau + t)(a_{1l}u + a_{2l}v) - \tau A_l)](1 - H(u)), \end{aligned} \tag{8}$$

where the coefficients in Eq. (8) can be determined by the reconstructed directional derivatives and compatibility condition

$$\langle a_1^k \rangle = \frac{\partial W_k}{\partial \boldsymbol{n}}, \langle a_2^k \rangle = \frac{\partial W_k}{\partial \boldsymbol{\tau}}, \langle a_1^k u + a_2^k v + A^k \rangle = 0,$$

$$\langle \overline{a}_1 \rangle = \frac{\partial \overline{W}}{\partial \boldsymbol{n}}, \langle \overline{a}_2 \rangle = \frac{\partial \overline{W}}{\partial \boldsymbol{\tau}}, \langle \overline{a}_1 u + \overline{a}_2 v + \overline{A} \rangle = 0,$$

where $k = l, r$, $\boldsymbol{n}$ and $\boldsymbol{\tau}$ are local normal and tangential direction and $\langle ... \rangle$ are the moments of the equilibrium g and defined by

$$\langle ... \rangle = \int g(...)\psi d\Xi.$$

The spatial derivatives will be obtained by the WENO reconstruction, which will be given later. More details of the gas-kinetic scheme can be found in [38].

In the scheme above, the grid velocity $\boldsymbol{U}^g$ can be arbitrary for the control volume. The Eulerian governing equation is obtained with $\boldsymbol{U}^g = 0$, and the Lagrangian form is obtained with $\boldsymbol{U}^g = \boldsymbol{U}$, where $\boldsymbol{U}$ is the fluid velocity. In this paper, the structured meshes are used in the moving mesh computation for simplicity, while the unstructured reconstruction is used to deal with the distorted meshes. The strategies of mesh velocity are given as follows

1. The mesh velocity is specified directly. This is the simplest type of mesh velocity and is mainly adopted in the accuracy tests in this paper.
2. The mesh velocity can be given by the fluid velocity, and the cell centered Lagrangian nodal solver is used [24]. Denote $\boldsymbol{U}_p$ as the vertex fluid velocity of control volume, $\boldsymbol{U}_c$ as cell averaged fluid velocity, $C(p)$ as the set of control volumes that share the common vertex p, the mesh velocity can be obtained by solving the following linear system

$$\sum_{c \in C(p)} \mathbb{M}_{pc} \boldsymbol{U}_p = \sum_{c \in C(p)} l_{pc} p_c \boldsymbol{n}_{pc} + \mathbb{M}_{pc} \boldsymbol{U}_c,$$

where

$$\mathbb{M}_{pc} = \rho_c a_c [l_{pc}^-(\boldsymbol{n}_{pc}^- \otimes \boldsymbol{n}_{pc}^-) + l_{pc}^+(\boldsymbol{n}_{pc}^+ \otimes \boldsymbol{n}_{pc}^+)],$$
$$l_{pc} \boldsymbol{n}_{pc} = l_{pc}^- \boldsymbol{n}_{pc}^- + l_{pc}^+ \boldsymbol{n}_{pc}^+,$$

where pp^- and pp^+ are the line segments of c that share the vertex p. l_{pc}^-, l_{pc}^+ and $\boldsymbol{n}_{pc}^-, \boldsymbol{n}_{pc}^+$ are the half lengthes and outer normal directions of the two segments. The matrix $\mathbb{M}_{pc}$ is symmetric positive definite. Therefore, the system will always admit a unique solution.
3. The mesh velocity can be determined by the variational approach [34], and the corresponding Euler-Lagrange equations can be obtained from

$$(\omega x_\xi)_\xi + (\omega x_\eta)_\eta = 0,$$
$$(\omega y_\xi)_\xi + (\omega y_\eta)_\eta = 0,$$

where (x, y) and (ξ, η) denote the physical and computational coordinates, ω is the monitor function and can be chosen as a function of the flow variables, such as the density, velocity, pressure, or their gradients. In the numerical tests, without no special statement, the monitor function takes the form

$$\omega = \sqrt{1 + \alpha |\nabla \rho|^2}.$$

The mesh distribution in the physical space can be directly generated, and more details can be found in [34].

Due to the features of moving-mesh methods, the structured meshes are adopted in the computations. In order to avoid mesh distortion, the new meshes obtained by the Lagrangian method and adaption method are smoothed by the following smooth procedure for the structured meshes

$$\widetilde{\boldsymbol{x}}_{ij}^{n+1} = (4\boldsymbol{x}_{ij}^{n+1} + \boldsymbol{x}_{i-1,j}^{n+1} + \boldsymbol{x}_{i+1,j}^{n+1} + \boldsymbol{x}_{i,j-1}^{n+1} + \boldsymbol{x}_{i,j+1}^{n+1})/8,$$

where $\boldsymbol{x}_{ij}^{n+1}$ is the coordinate of the grid points obtained above. This procedure is conducted for some certain steps. With the smoothed mesh, the grid velocity $\boldsymbol{U}_{ij}^g = (U_{ij}^g, V_{ij}^g)$ can be determined as follows

$$\boldsymbol{U}_{ij}^g = \frac{\widetilde{\boldsymbol{x}}_{ij}^{n+1} - \boldsymbol{x}_{ij}^n}{\Delta t}.$$

The mesh velocities at Gaussian quadrature points can be obtained by the linear interpolation of mesh velocity at the grid points. For each Gaussian quadrature points, the constant mesh velocity is also used in the time interval $[t_n, t_n + \Delta t]$.

3. Two-stage temporal discretization

A two-stage fourth-order temporal discretization was developed for Lax-Wendroff flow solvers, such as the generalized Riemann problem (GRP) solver [2] and the gas-kinetic scheme [22]. Consider the following time-dependent equation

$$\frac{\partial \boldsymbol{w}}{\partial t} = \mathcal{L}(\boldsymbol{w}), \tag{9}$$

with the initial condition at t_n, i.e.,

$$\boldsymbol{w}(t = t_n) = \boldsymbol{w}^n,$$

where $\mathcal{L}$ is an operator for spatial derivative of flux. Introducing an intermediate state at $t^* = t_n + \Delta t/2$,

$$\boldsymbol{w}^* = \boldsymbol{w}^n + \frac{1}{2} \Delta t \mathcal{L}(\boldsymbol{w}^n) + \frac{1}{8} \Delta t^2 \frac{\partial}{\partial t} \mathcal{L}(\boldsymbol{w}^n), \tag{10}$$
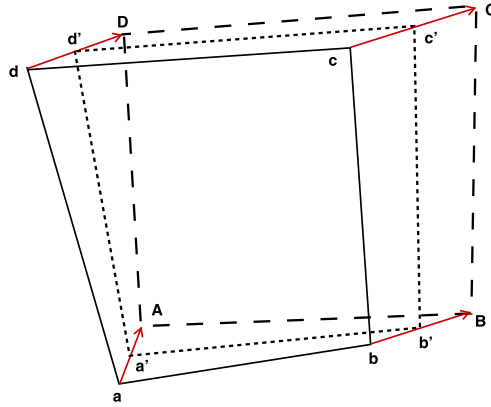
Fig. 2. Schematic for a moving control volume: $\Omega(t^*) = [a'b'c'd']$ is the intermediate one at $t^* = t_n + \Delta t/2$ and a', b', c', d' are the mid-points of aA, bB, cC, dD.

the state $\boldsymbol{w}$ at $t_{n+1} = t_n + \Delta t$ can be updated with the following formula

$$\boldsymbol{w}^{n+1} = \boldsymbol{w}^n + \Delta t \mathcal{L}(\boldsymbol{w}^n) + \frac{1}{6}\Delta t^2 \Big(\frac{\partial}{\partial t}\mathcal{L}(\boldsymbol{w}^n) + 2\frac{\partial}{\partial t}\mathcal{L}(\boldsymbol{w}^*)\Big). \tag{11}$$

It can be proved that Eq. (10) and Eq. (11) provide a fourth-order time accurate solution for Eq. (9) at $t = t_n + \Delta t$. The details of proof can be found in [23].

To achieve the high-order spatial and temporal accuracy, the two-stage temporal discretization can be extended to the moving mesh computation Eq. (4), where the operator $\mathcal{L}$ is denoted as

$$\mathcal{L}(\Omega_i, W_i) = -\sum_m F_{im}(t).$$

As shown in Fig. 2, the coordinate of the local moving reference and the length of cell interface are both time-dependent, which is critical for accuracy and geometry conservation law. In the two-stage method, the variables are defined and the reconstruction is performed at t_n and $t^* = t_n + \Delta t/2$, respectively. Due to the constant velocity for each vertex, the intermediate control volume at t^* moves to $\Omega(t^*) = [a'b'c'd']$ exactly, where a', b', c', d' are the mid-points of aA, bB, cC, dD. To implement the two-stage method, the WENO reconstruction is performed with the re-distributed meshes at t_n and t^*. With the reconstructed variables, $\mathcal{L}(W)$ and temporal derivative $\partial_t \mathcal{L}(W)$ for Ω_i at t_n can be written as

$$\mathcal{L}(\Omega_i^n, W_i^n) = -\sum_m \sum_p \omega_{m_p} F_{i,m_p}^n |\Gamma_{im}^X|,$$

$$\partial_t \mathcal{L}(\Omega_i^n, W_i^n) = -\sum_m \sum_p \omega_{m_p} (\partial_t F_{i,m_p}^n |\Gamma_{im}^X| + (F')_{i,m_p}^n |\Gamma_{im}^U|),$$

where F_{i,m_p}^n and $\partial_t F_{i,m_p}^n$ can be given by the linear combination of $\widetilde{F}_{i,m_p}^n$ and $\partial_t \widetilde{F}_{i,m_p}^n$ according to Eq. (6). To determine the coefficients $\widetilde{F}_{i,m_p}^n$ and $\partial_t \widetilde{F}_{i,m_p}^n$, the time dependent numerical flux in the local coordinate can be expanded as the linear form

$$\widetilde{F}_{i,m_p}(t) = \widetilde{F}_{i,m_p}^n + \partial_t \widetilde{F}_{i,m_p}^n (t - t_n). \tag{12}$$

Integrating Eq. (12) over $[t_n, t_n + \Delta t/2]$ and $[t_n, t_n + \Delta t]$, we have the following two equations

$$\widetilde{F}_{i,m_p}^n \Delta t + \frac{1}{2}\partial_t \widetilde{F}_{i,m_p}^n \Delta t^2 = \widehat{\mathbb{F}}(\boldsymbol{x}_{i,m_p}, \Delta t),$$

$$\frac{1}{2}\widetilde{F}_{i,m_p}^n \Delta t + \frac{1}{8}\partial_t \widetilde{F}_{i,m_p}^n \Delta t^2 = \widehat{\mathbb{F}}(\boldsymbol{x}_{i,m_p}, \Delta t/2),$$

where

$$\widehat{\mathbb{F}}(\boldsymbol{x}_{i,m_p}, \delta) = \int_{t_n}^{t_n+\delta} \widetilde{F}_{i,m_p}(t)\mathrm{d}t = \iint_{t_n}^{t_n+\delta} \widetilde{u}\widetilde{\psi} f(\boldsymbol{x}_{i,m_p}, t, \widetilde{\boldsymbol{u}}, \xi)\mathrm{d}\Xi\mathrm{d}t.$$

The coefficients $\widetilde{F}_{i,m_p}^n$ and $\partial_t \widetilde{F}_{i,m_p}^n$ can be determined by solving the linear system. Similarly, $\mathcal{L}(\Omega_i^*, W_i^*)$ and temporal derivative $\partial_t \mathcal{L}(\Omega_i^*, W_i^*)$ at the intermediate state can be constructed as well. More details of the two-stage fourth-order scheme
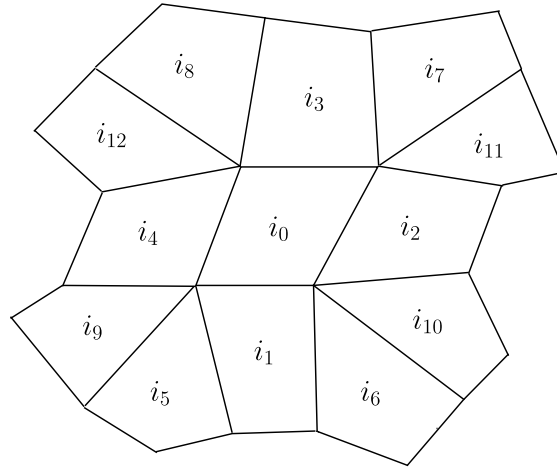
Fig. 3. Stencils for third-order schemes on quadrilateral meshes.

can be found in [23,27]. In the moving-mesh procedure, the geometrical conservation law (GCL) need to be considered. Generally, the preservation of free stream is often referred as the geometric conservation law, which means that a uniform flow on a grid that moves arbitrarily in space as a function of time must be preserved for any numerical discretization scheme [35,31,25]. As shown in Fig. 2, the segment ab is considered as example, and the quadrilateral $abb'a'$ is swept by ab during a time interval $[t_n, t_n + \Delta t]$. (U_a^g, V_a^g) and (U_b^g, V_b^g) are denoted as the grid velocity in local coordinate of Γ_{ab}. The area of $abBA$ can be also calculate from location of four vertexes

$$V_{abBA} = \frac{1}{2}(U_a^g + U_b^g)|\Gamma_{ab}^X|\Delta t + \frac{1}{2}(U_a^g V_b^g - U_b^g V_a^g)\Delta t^2, \tag{13}$$

where $|\Gamma_{ab}^X|$ is the length of ab. Meanwhile, for stationary uniform flow with $\rho = 1$, we have $\partial_t F_{i,m_p}^n = 0$ and $F_{i,m_p}^\rho = -\rho \boldsymbol{U}_{i,m_p}^g$. Eq. (13) can be also rewritten by the Gaussian quadrature

$$V_{abBA} = -\sum_p \omega_{m_p}\left(F_{i,m_p}^n|\Gamma_{ab}^X|\Delta t + \frac{1}{2}(F')_{i,m_p}|\Gamma_{ab}^U|\Delta t^2\right),$$

where $|\Gamma_{ab}^U| = |U_a U_b|$ and

$$-F_{i,m_p}^\rho|\Gamma_{im}^X| = U_{i,m_p}^g(y_b - y_a) - V_{i,m_p}^g(x_b - x_a) = \boldsymbol{U}_{i,m_p}^g \cdot \boldsymbol{n}_\perp|\Gamma_{ab}^X|,$$
$$-(F')_{i,m_p}^\rho|\Gamma_{im}^U| = U_{i,m_p}^g(V_b - V_a) - V_{i,m_p}^g(U_b - U_a) = \boldsymbol{U}_{i,m_p}^g \cdot \boldsymbol{n}'_\perp|\Gamma_{ab}^U|.$$

Therefore, another flux $(F')_{i,m_p}$ needs to be calculated and the GCL can be preserved. More studies about GCL will be invested in the future.

Remark 1. With the two-stage method, the moving-mesh technique can be extended the three-dimensional hexahedron meshes. For the three-dimensional flows, the cell with non-coplanar vertexes may be commonly generated. The trilinear interpolation is used to parameterize the hexahedron, and the bilinear interpolation is used to parameterize the interface of hexahedron. More details can be found in [30].

4. WENO reconstruction

During the moving-mesh procedure, the mesh becomes distorted even with the structured meshes, and the development of robust high-order scheme on a low quality mesh is demanding. Recently, a third-order WENO reconstruction is constructed on quadrilateral meshes [40], in which high-order accuracy is achieved and robustness is improved. In this section, we briefly review such scheme with unstructured stencil, and the extension to the structured mesh is straightforward. The unstructured version for moving-mesh computation will be developed in the future for the problem with complicated geometry.

To achieve the third-order accuracy, a general selection of stencil is given in Fig. 3 and the following quadratic polynomial $P^2(x, y)$ can be constructed

$$P^2(x, y) = W_{i_0} + \sum_{k=1}^{5} a_k p^k(x, y), \tag{14}$$

where W_{i_0} is the cell average value of $W(x, y)$ over cell Ω_{i_0} and $p^k(x, y), k = 1, ..., 5$ are basis functions, which are given as follows

$$\begin{cases} p^1(x, y) = x - \dfrac{1}{|\Omega_{i_0}|} \iint\limits_{\Omega_{i_0}} x \mathrm{d}x \mathrm{d}y, \\[2mm] p^2(x, y) = y - \dfrac{1}{|\Omega_{i_0}|} \iint\limits_{\Omega_{i_0}} y \mathrm{d}x \mathrm{d}y, \\[2mm] p^3(x, y) = x^2 - \dfrac{1}{|\Omega_{i_0}|} \iint\limits_{\Omega_{i_0}} x^2 \mathrm{d}x \mathrm{d}y, \\[2mm] p^4(x, y) = y^2 - \dfrac{1}{|\Omega_{i_0}|} \iint\limits_{\Omega_{i_0}} y^2 \mathrm{d}x \mathrm{d}y, \\[2mm] p^5(x, y) = xy - \dfrac{1}{|\Omega_{i_0}|} \iint\limits_{\Omega_{i_0}} xy \mathrm{d}x \mathrm{d}y. \end{cases} \tag{15}$$

With the following constraint over the cell $\Omega_{i_j}, i_j \in S = \{i_0, i_1, ..., i_{12}\}$,

$$\frac{1}{|\Omega_{i_j}|} \int\limits_{\Omega_{i_j}} P^2(x, y) \mathrm{d}x \mathrm{d}y = W_{i_j},$$

the coefficients $\mathbf{a} = (a_1, ..., a_5)$ in Eq. (14) can be fully given, where W_{i_j} is the cell averaged variables over cell Ω_{i_j}. Similar with the standard WENO reconstruction [13], twelve sub-stencils $S_j, j = 1, ..., 12$ are selected from the large stencil given in Fig. 3

$$\begin{aligned} & P_1^1 \text{ on } S_1 = \{i_0, i_1, i_2\}, \quad P_2^1 \text{ on } S_2 = \{i_0, i_2, i_3\}, \quad P_3^1 \text{ on } S_3 = \{i_0, i_3, i_4\}, \\ & P_4^1 \text{ on } S_4 = \{i_0, i_4, i_1\}, \quad P_5^1 \text{ on } S_5 = \{i_0, i_1, i_5\}, \quad P_6^1 \text{ on } S_6 = \{i_0, i_1, i_6\}, \\ & P_7^1 \text{ on } S_7 = \{i_0, i_3, i_7\}, \quad P_8^1 \text{ on } S_8 = \{i_0, i_3, i_8\}, \quad P_9^1 \text{ on } S_9 = \{i_0, i_4, i_9\}, \\ & P_{10}^1 \text{ on } S_{10} = \{i_0, i_2, i_{10}\}, P_{11}^1 \text{ on } S_{11} = \{i_0, i_2, i_{11}\}, P_{12}^1 \text{ on } S_{12} = \{i_0, i_4, i_{12}\}. \end{aligned}$$

Twelve candidate linear polynomials P_j^1 corresponding to the candidate sub-stencils can be constructed as follows

$$\frac{1}{|\Omega_{S_{j,k}}|} \int\limits_{\Omega_{S_{j,k}}} P_j^1(x, y) \mathrm{d}x \mathrm{d}y = W_{S_{j,k}}, \ k = 0, 1, 2,$$

where $\Omega_{S_{j,k}}$ is the $(k+1)$-th cell in the sub-stencils S_j, and $W_{S_{j,k}}$ is the cell averaged value over cell $\Omega_{S_{j,k}}$.

With point value of the quadratic polynomial $P^2(x, y)$ and linear polynomials P_j^1 at the Gaussian quadrature point (x_G, y_G), a standard procedure of WENO scheme is adopted to obtain the linear weights γ_j [13]. However, in the traditional WENO reconstruction, the very large linear weights and negative weights appear with the lower mesh quality. In order to improve the robustness of WENO schemes, an optimization approach is given to deal with the very large linear weights. The weighting parameters is introduced for each cell, such that the ill cell contributes little to the quadratic polynomial in Eq. (14). For quadrilateral meshes, the weighting parameters are defined for each cell

$$\begin{cases} d_j = 1, & j = 1, ..., 4, \\[2mm] d_j = \dfrac{1}{\max(1, |\gamma_j|)}, & j = 5, ..., 12. \end{cases}$$

The optimized coefficients $\mathbf{a} = (a_1, ..., a_5)$ of the quadratic polynomial in Eq. (14) are given by the following weighted linear system

$$\sum_{k=1}^{5} d_j \cdot A_{jk} a_k = d_j \cdot (W_{i_j} - W_{i_0}).$$

With the procedure above, the maximum γ_j becomes the order $O(1)$ [40].

To deal with the negative linear weights, the splitting technique [33] is considered for the optimized approach as follows

$$\widetilde{\gamma}_j^+ = \frac{1}{2}(\gamma_j + \theta \, |\gamma_j|), \ \ \widetilde{\gamma}_j^- = \widetilde{\gamma}_j^+ - \gamma_j,$$

where $\theta = 3$ is taken in numerical tests. The scaled non-negative linear weights $\gamma_j^\pm$ and nonlinear weights $\delta_j^\pm$ are given by

$$\gamma_j^\pm = \frac{\widetilde{\gamma}_j^\pm}{\sigma^\pm}, \, \sigma^\pm = \sum_j \widetilde{\gamma}_j^\pm,$$

$$\delta_j^\pm = \frac{\alpha_j^\pm}{\sum_{l=1} \alpha_l^\pm}, \, \alpha_j^\pm = \frac{\gamma_j^\pm}{(\widetilde{\beta}_j^\pm + \epsilon)^2},$$

where ϵ is a small positive number, $\widetilde{\beta}_j^{\,\pm}$ is a new smooth indicator defined on unstructured meshes

$$\widetilde{\beta}_j^{\,\pm} = \beta_j\big(1 + \gamma_j^\pm \beta_j + (\gamma_j^\pm \beta_j)^2\big),$$

where β_j is defined as

$$\beta_j = \sum_{|\alpha|=1}^{K} |\Omega|^{|\alpha|-1} \iint_\Omega \big(D^\alpha P_j^1(x, y)\big)^2 \mathrm{d}x\mathrm{d}y,$$

α is a multi-index, and D is the derivative operator. With the new smooth indicator, the accuracy keeps the original order in smooth regions with $IS = h^2(1 + O(h))$. The final reconstructed variables at the Gaussian quadrature point can be written as

$$R(x_G, y_G) = \sum_j (\delta_j^+ P_j^1(x_G, y_G) - \delta_j^- P_j^1(x_G, y_G)).$$

Compared with the traditional high-order schemes with Riemann solvers, an extra reconstruction for the equilibrium state is needed. With the reconstructed variables W_l and W_r at both sides of cell interface, the variables at the cell interface can be determined by the compatibility condition Eq. (2) as follows

$$\int \psi g_G \mathrm{d}\Xi = W_G = \int_{u>0} \psi g_l \mathrm{d}\Xi + \int_{u<0} \psi g_r \mathrm{d}\Xi, \tag{16}$$

where g_l and g_r are the equilibrium states corresponding to W_l and W_r respectively. To third-order accuracy, the Taylor expansion corresponding to equilibrium state at the Gaussian quadrature point is expressed as

$$\overline{W}(x, y) = W_G + \overline{W}_{\boldsymbol{n}}(x - x_G) + \overline{W}_{\boldsymbol{\tau}}(y - y_G)$$
$$+ \frac{1}{2}\overline{W}_{\boldsymbol{nn}}(x - x_G)^2 + \overline{W}_{\boldsymbol{n\tau}}(x - x_G)(y - y_G) + \frac{1}{2}\overline{W}_{\boldsymbol{\tau\tau}}(y - y_G)^2,$$

where $\boldsymbol{n}, \boldsymbol{\tau}$ are local normal and tangential directions. With the following constrains

$$\frac{1}{|\Omega_{i_j}|} \int_{\Omega_{i_j}} \overline{W}(x, y)\mathrm{d}x\mathrm{d}y = W_{i_j}, i_j \in T = \{i_0, i_1, ..., i_7\},$$

the spatial derivatives can be obtained by the least square methods, where the stencil for equilibrium state reconstruction is given in Fig. 4. For most mesh generation method, there are at least five elements in the above stencil, which guarantees the least square method solvable. Based on the spatial reconstructions, the reconstructed variables and the gas distribution functions in the local moving coordinate can be obtained, and the flow variables can be updated by the two-stage framework.

Remark 2. The current scheme improves robustness of classical WENO scheme and works well for two-dimensional flows. However, the selection of stencils becomes more complicated for three-dimensional flows. In addition, the linear weights need to be calculated twice every stage, which reduces the efficiency greatly. With the newly developed gas-kinetic scheme with WENO-AO reconstruction [30], the time independent linear weights are used and the reconstructed polynomial over the whole control can be given. Thus, the reconstruction procedure as well as the gas-kinetic flux solver can be simplified greatly.
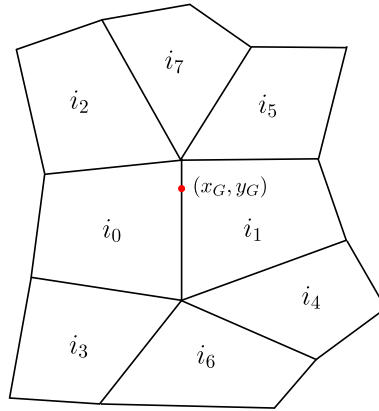
Fig. 4. Stencils for equilibrium state of third-order scheme on quadrilateral meshes.

5. Numerical tests

In this section, numerical tests for both inviscid and viscous flows are presented to validate our numerical scheme. For the inviscid flow, the collision time τ takes

$$\tau = \epsilon \Delta t + C | \frac{p_l - p_r}{p_l + p_r} | \Delta t,$$

where $\epsilon = 0.01$ and $C = 1$. For the viscous flow, we have

$$\tau = \frac{\mu}{p} + C | \frac{p_l - p_r}{p_l + p_r} | \Delta t,$$

where p_l and p_r denote the pressure on the left and right sides of the cell interface, μ is the dynamic viscous coefficient, and p is the pressure at the cell interface. The ratio of specific heats takes $\gamma = 1.4$. To validate the WENO based gas-kinetic scheme, the accuracy test on the unstructured quadrilateral meshes is presented with the stationary mesh first. For the moving-mesh computation, the structured meshes are used to avoid the distortion of computational mesh, while the procedure of reconstruction is still based on the unstructured code. The flow chart for the high-order ALE scheme is presented in Fig. 5. In order to eliminate the spurious oscillation and improve the stability, the reconstruction can be performed for the characteristic variables. The characteristic variables are defined as $\omega = R^{-1}W$, where R is the right eigenmatrix of Jacobian matrix $n_x(\partial F/\partial W)_G + n_y(\partial G/\partial W)_G$ at Gaussian quadrature point. With the reconstructed values, the conservative variables can be obtained by the inverse projection.

5.1. Accuracy tests

The first accuracy test is two-dimensional advection of density perturbation. The computational domain is $[0, 2] \times [0, 2]$ and the initial conditions are given as follows

$$\rho_0(x, y) = 1 + 0.2 \sin(\pi (x + y)), \ p_0(x, y) = 1,$$
$$U_0(x, y) = 1, \ V_0(x, y) = 1.$$

The periodic boundary conditions are imposed at boundaries and the exact solutions are

$$\rho(x, y, t) = 1 + 0.2 \sin(\pi (x + y - t)), \ p(x, y, t) = 1,$$
$$U(x, y, t) = 1, \ V(x, y, t) = 1.$$

The accuracy on unstructured quadrilateral and triangular meshes are tested, and the mesh with cell size $h = 1/16$ is given in Fig. 6 as reference. The L^1 and L^2 errors and convergence orders are presented in Table 1 and Table 2, and the expected order is achieved. For the accuracy with moving-mesh, the structured meshes are used. Three kinds of time dependent meshes are given

$$\text{Type-1}: \begin{cases} x(t) = x_0 + 0.05 \sin \pi t \sin \pi x_0 \sin \pi y_0, \\ y(t) = y_0 + 0.05 \sin \pi t \sin \pi x_0 \sin \pi y_0. \end{cases} \tag{17}$$
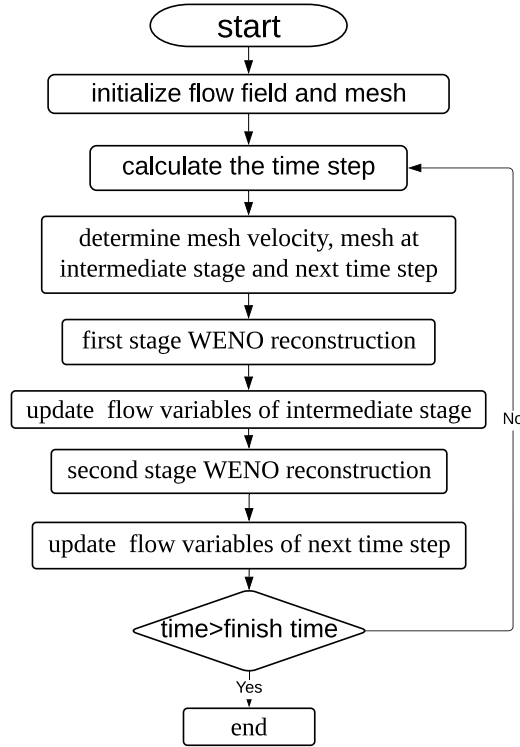
Fig. 5. Flow chart of high-order ALE gas-kinetic scheme.
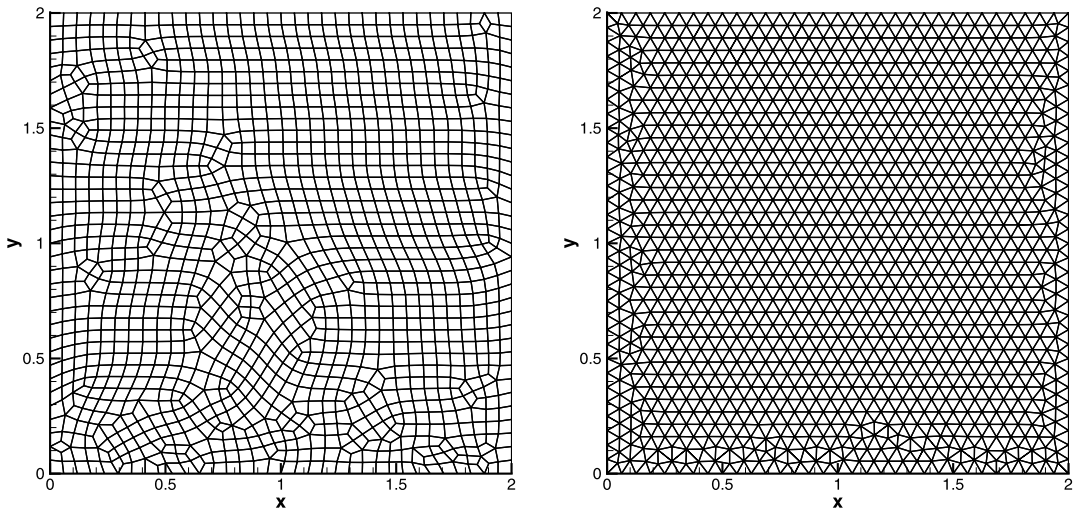

Fig. 6. Advection of density perturbation: quadrilateral and triangular meshes with $h = 1/16$.

$$\text{Type-2}: \begin{cases} x(t) = x_0 + 0.05 \sin \pi t \sin 2\pi x_0 \sin 2\pi y_0, \\ y(t) = y_0 + 0.05 \sin \pi t \sin 2\pi x_0 \sin 2\pi y_0. \end{cases} \tag{18}$$

$$\text{Type-3}: \begin{cases} x(t) = x_0 + 0.05 \sin \pi t \sin \pi x_0, \\ y(t) = y_0 + 0.05 \sin \pi t \sin \pi y_0, \end{cases} \tag{19}$$

where (x_0, y_0) is denoted as the initial mesh. The mesh velocity can be directly given during a time step. Initially, $N \times N$ cells are distributed uniformly. The L^1 and L^2 errors and orders of accuracy at $t = 2$ with N^2 cells are presented in Table 3, Table 4 and Table 5 for three types of moving-mesh, and the computational meshes with largest deformation at $t = 0.5$

Table 1
Advection of density perturbation: WENO-3rd on quadrilateral meshes.

mesh	L^1 error	Order	L^2 error	Order
1/8	1.3752E-02		1.5288E-02	
1/16	1.4112E-03	3.28	1.5684E-03	3.28
1/32	2.0183E-04	2.80	2.2400E-04	2.80
1/64	2.3544E-05	3.09	2.6098E-05	3.10

Table 2
Advection of density perturbation: WENO-3rd on triangular meshes.

mesh	L^1 error	Order	L^2 error	Order
1/8	4.8752E-03		5.4117E-03	
1/16	6.4576E-04	2.92	7.1650E-04	2.92
1/32	8.2542E-05	2.97	9.1507E-05	2.97
1/64	1.0308E-05	3.00	1.1427E-05	3.00

Table 3
Advection of density perturbation: L^1 and L^2 errors and orders for moving-mesh Type-1.

mesh	L^1 error	Order	L^2 error	Order
20^2	3.2472E-02		1.7989E-02	
40^2	4.2331E-03	2.93	2.3494E-03	2.93
80^2	5.3331E-04	2.98	2.9571E-04	2.99
160^2	6.6761E-05	2.99	3.7016E-05	2.99

Table 4
Advection of density perturbation: L^1 and L^2 errors and orders for moving-mesh Type-2.

mesh	L^1 error	Order	L^2 error	Order
20^2	3.3873E-02		1.8770E-02	
40^2	4.5521E-03	2.89	2.5410E-03	2.88
80^2	5.7874E-04	2.97	3.2386E-04	2.97
160^2	7.2641E-05	2.99	4.0674E-05	2.99

Table 5
Advection of density perturbation: L^1 and L^2 errors and orders for moving-mesh Type-3.

mesh	L^1 error	Order	L^2 error	Order
20^2	3.2267E-02		1.8112E-02	.
40^2	4.2342E-03	2.9298	2.3846E-03	2.9251
80^2	5.3338E-04	2.9888	3.0062E-04	2.9877
160^2	6.6778E-05	2.9977	3.7644E-05	2.9974

are shown in Fig. 7. As reference, the errors and orders of accuracy with stationary meshes are also given in Table 6. The expected order of accuracy is well kept with the moving-mesh procedure.

The second one is isotropic vortex propagation problem, which is a non-linear case for accuracy test. The mean flow is $(\rho, u, v, p) = (1, 1, 1, 1)$, and an isotropic vortex is added to the mean flow, i.e., with perturbation in u, v and temperature $T = p/\rho$, and no perturbation in entropy $S = p/\rho^\gamma$. The perturbation is given by

$$(\delta u, \delta v) = \frac{\epsilon}{2\pi} e^{\frac{(1-r^2)}{2}} (-y, x),$$

$$\delta T = -\frac{(\gamma - 1)\epsilon^2}{8\gamma \pi^2} e^{1-r^2}, \delta S = 0,$$

where $r^2 = x^2 + y^2$ and the vortex strength $\epsilon = 5$. The computational domain is $[0, 10] \times [0, 10]$, the periodic boundary conditions are imposed on the boundaries in both x and y directions. The exact solution is the perturbation which propagates with the velocity $(1, 1)$. For the accuracy with moving-mesh velocity, the following time dependent meshes are considered as follows

$$\text{Type-III} : \begin{cases} x(t) = x_0 + 0.05 \sin 0.2\pi t \sin \pi x_0 \sin \pi y_0, \\ y(t) = y_0 + 0.05 \sin 0.2\pi t \sin \pi x_0 \sin \pi y_0, \end{cases}$$
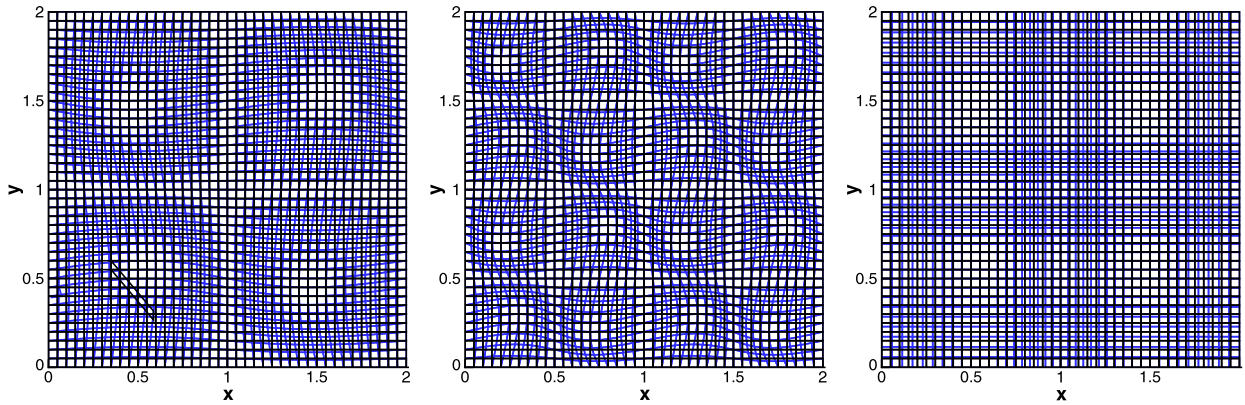
Fig. 7. Advection of density perturbation: computational mesh with 40^2 cells at $t = 0.5$ for moving-mesh Type-1, Type-2 and Type-3.

Table 6
Advection of density perturbation: L^1 and L^2 errors and orders with stationary meshes.

mesh	L^1 error	Order	L^2 error	Order
20^2	3.1442E-02		1.7398E-02	
40^2	4.0849E-03	2.94	2.2654E-03	2.98
80^2	5.1443E-04	2.94	2.8496E-04	2.99
160^2	6.4388E-05	2.99	3.5669E-05	2.99

Table 7
Isotropic vortex propagation: L^2 errors and orders for stationary meshes (left) and moving-meshes (right).

mesh	stationary meshes		moving-meshes	
	L^2 error	Order	L^2 error	Order
40^2	7.4765E-02		7.5223E-02	
80^2	1.2993E-02	2.5245	1.3235E-02	2.5067
160^2	1.8030E-03	2.8492	1.8555E-03	2.8345
320^2	2.2982E-04	2.9718	2.5870E-04	2.8424

where (x_0, y_0) is denoted as the initial mesh. Initially, the $N \times N$ cells are uniformly distributed. The mesh velocity can be directly given during a time step. The L^2 errors and orders at $t = 10$ are presented in Table 7. As reference, the errors and orders of accuracy with stationary meshes are also given in Table 7. The expected accuracy is obtained with the moving-mesh procedure as well. The density distributions for moving-mesh with 80×80 cells at $t = 2.5$ and 7.5 are also given in Fig. 8, where the vortex is well preserved with the moving-mesh procedure.

5.2. Geometric conservation law

The geometric conservation law (GCL) is also tested by the time dependent meshes. The computational domain is $[0, 2] \times [0, 2]$, and the initial condition is

$$\rho_0(x, y) = 1, \ p_0(x, y) = 1, \ U_0(x, y) = 1, \ V_0(x, y) = 1.$$

The periodic boundary conditions are adopted as well. The time dependent meshes are given by Eq. (17), Eq. (18) and Eq. (19). The L^1 and L^2 errors at $t = 2$ with N^2 cells are given in Table 8 for three types of moving-mesh. The errors reduce to the machine zero. The geometric conservation law is well preserved by the current scheme.

5.3. One dimensional Riemann problems

In this case, the one-dimensional Riemann problems are tested. The first one is Sod problem, and the initial condition is given as follows

$$(\rho, U, p) = \begin{cases} (1, 0, 1), & 0 \leq x < 0.5, \\ (0.125, 0, 0.1), & 0.5 \leq x \leq 1. \end{cases}$$

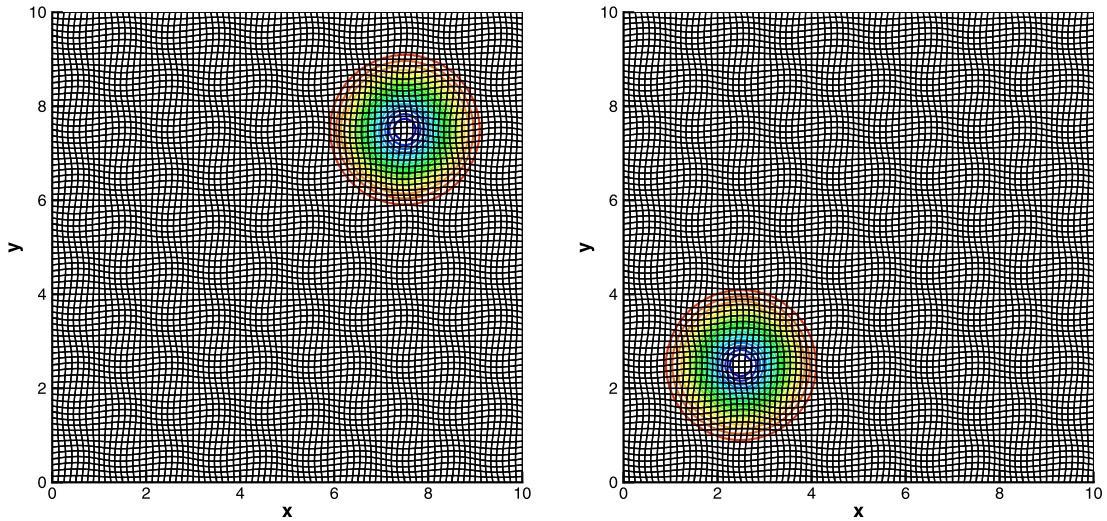The second one is Lax problem, and the initial condition is given as follows

Fig. 8. Isotropic vortex propagation: density distributions for moving-mesh with 80×80 cells at $t = 2.5$ and 7.5.

Table 8
Accuracy test: geometric conservation law for mesh velocities Type-I and Type-II.

mesh	mesh Type-1		mesh Type-2		mesh Type-3	
	L^1 error	L^2 error	L^1 error	L^2 error	L^1 error	L^2 error
10^2	8.51E-15	5.31E-15	9.20E-15	5.72E-15	2.33E-14	1.51E-14
20^2	1.90E-14	1.22E-14	2.03E-14	1.27E-14	5.08E-14	3.34E-14
40^2	4.65E-14	3.01E-14	4.49E-14	2.90E-14	6.85E-14	4.27E-14
80^2	9.32E-14	5.99E-14	1.02E-13	6.69E-14	2.43E-13	1.58E-13
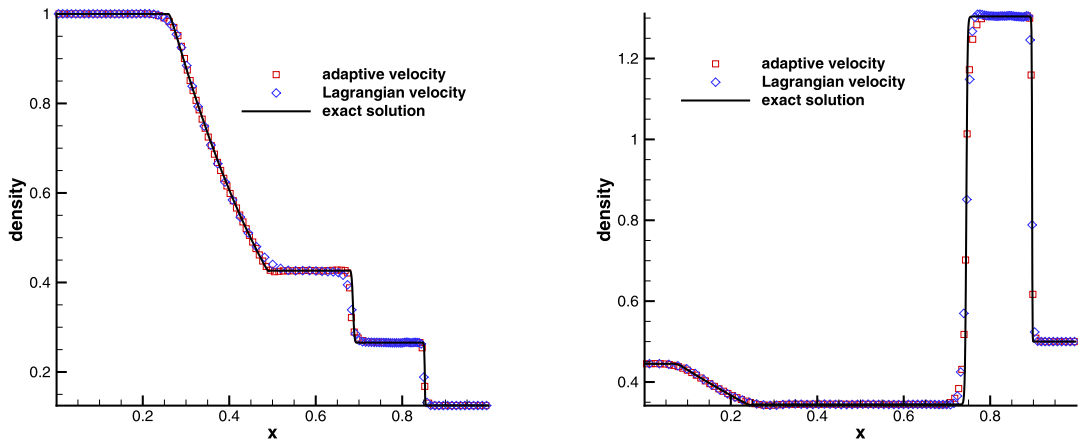
Fig. 9. One dimensional Riemann problem: the density distributions for Sod problem at $t = 0.2$ (left) and Lax problem at $t = 0.16$ (right).

$$(\rho, U, p) = \begin{cases} (0.445, 1.198, 3.528), & 0 \leq x < 0.5 \\ (0.5, 0.5, 0.571), & 0.5 \leq x \leq 1. \end{cases}$$

In the computation, these two cases are tested in the domain $[0, 1] \times [0, 0.1]$ and non-reflection boundary condition is adopted at the boundaries of computational domain. Initially, 100×10 cells are equally distributed. The adaptation velocity and Lagrangian velocity are chosen as mesh velocities. For the adaptive procedure, the parameter α in the monitor function takes 0.1 for Sod problem and 0.02 for Lax problem. The density distributions for Sod problem at $t = 0.2$ and Lax problem at $t = 0.16$ with $x = 0$ are presented in Fig. 9. The histories of mesh distribution from adaptation velocity and Lagrangian velocity are presented in Fig. 10 and Fig. 11. The numerical solutions agree well with the exact solutions. Due the local mesh adaptation, the discontinuities are well resolved by the current scheme. For the one-dimensional case, the grid velocity can given by the compatibility condition Eq. (16), which also works well for the Riemann problems.
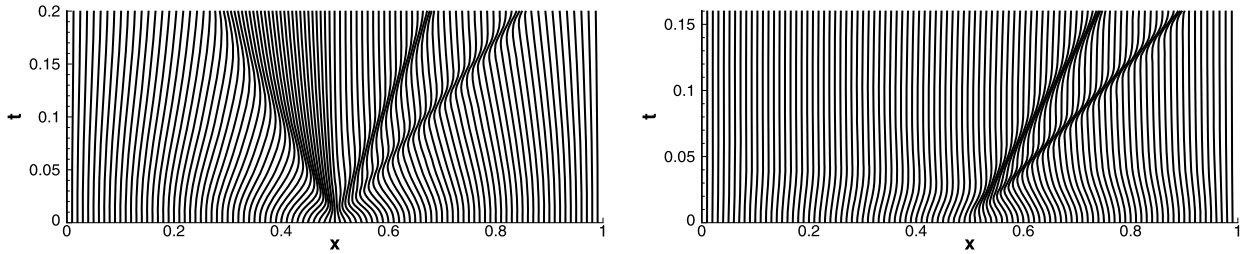
Fig. 10. One dimensional Riemann problem: the mesh evolution with adaptation velocity for Sod problem (left) and Lax problem (right).
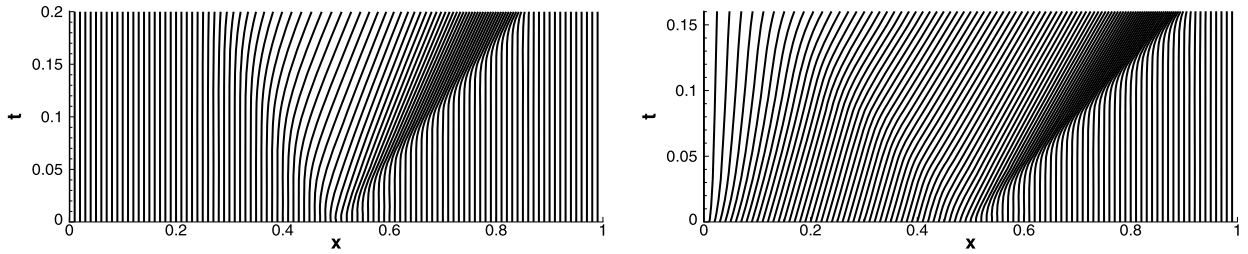

Fig. 11. One dimensional Riemann problem: the mesh evolution with Lagrangian velocity for Sod problem (left) and Lax problem (right).
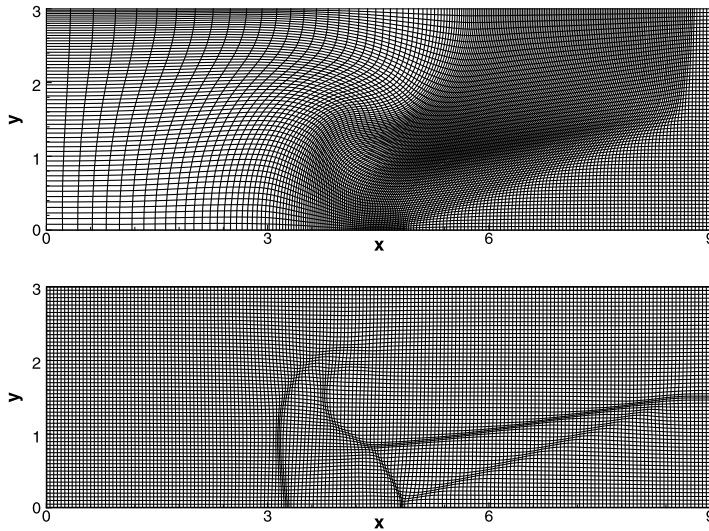

Fig. 12. Triple-point problem: the mesh distribution with 180×60 cells with Larangian velocity (top) and adaptation velocity (bottom).

5.4. Triple-point problem

The triple-point problem was widely used to validate to the performance of Larangian and ALE methods with large mesh deformation [11,19]. The initial condition is given as follows

$$(\rho, U, V, p) = \begin{cases} (1, 0, 0, 1), & (x, y) \in D_1 = [0, 1] \times [0, 3], \\ (0.125, 0, 0, 0.1), & (x, y) \in D_2 = [1, 9] \times [0, 1.5], \\ (1, 0, 0, 0.1), & (x, y) \in D_3 = [1, 9] \times [1.5, 3]. \end{cases}$$

The non-reflective boundary conditions are used at all boundaries. Left from $x = 1$, a high pressure is located in D_1, which generates a shock wave propagating to the right, and no waves are generated at the beginning at the domain $D_2 \cup D_3$. Initially, $3N \times N$ cells are equally distributed. The adaptation velocity and Lagrangian velocity are chosen as mesh velocities. For the adaptive procedure, the parameter α in the monitor function takes 0.05. The mesh distribution with 180×60 cells for Larangian and adaptation velocity at $t = 4$ are presented in Fig. 12. The density distribution with 180×60 cells for Larangian and adaptation velocity are given in Fig. 13, where a vortex appears and swirls the flows around the triple point

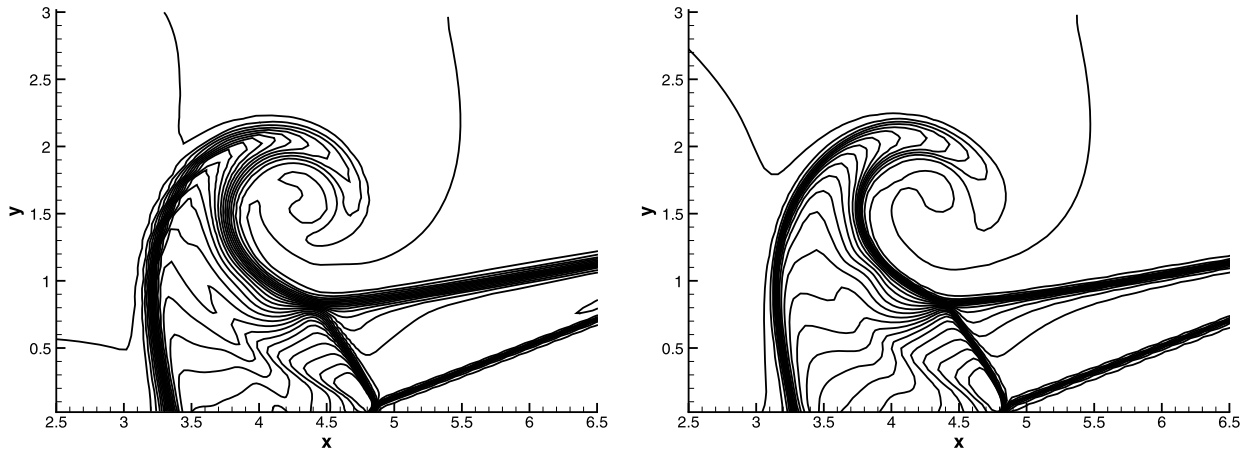**Fig. 13.** Triple-point problem: the density distribution with Larangian velocity (left) and (right) adaptation velocity with 180×60 cells.

due to the different shock speeds over the vertical line. With the local mesh refinement, the interaction of contacts can be well captured.

5.5. Two-dimensional Riemann problems

In this case, the two-dimensional Riemann problems for Euler equations are presented [21]. The computation domain is $[0, 1] \times [0, 1]$ and the non-reflection condition is used for the boundaries, and $N \times N$ cells are equally distributed initially. The adaptation velocity is chosen as mesh velocity. The initial condition is given as follows

$$(\rho, U, V, p) = \begin{cases} (1, 0.75, -0.5, 1), & x > 0.5, y > 0.5, \\ (2, 0.75, 0.5, 1), & x < 0.5, y > 0.5, \\ (1, -0.75, 0.5, 1), & x < 0.5, y < 0.5, \\ (3, -0.75, -0.5, 1), & x > 0.5, y < 0.5. \end{cases}$$

This case is the interaction of four contact discontinuities with same signs $J_{12}^- J_{32}^- J_{41}^- J_{34}^-$, where J_{lr}^- represents the negative contact discontinuity connecting the l and r areas

$$J_{lr}^- : w_l = w_r, p_l = p_r, w_l' \geq w_r',$$

where w_l, w_r are the normal velocities and w_l', w_r' are the tangential velocities. The parameter α in the monitor function takes 0.1. The density distribution and computational mesh with 100×100 cells are given in Fig. 14 at $t = 0.4$. The density distribution with 400×400 cells is given in Fig. 15. For this case, the instantaneous interaction of contacts results in a complex wave pattern, and the instability of shear appears due to the local mesh adaptation and mesh refinement. As a reference, the numerical results with stationary mesh is given in Fig. 15 as well. The nonlinear combination of linear polynomial smears the discontinuities.

5.6. Viscous shock tube

This problem was introduced to test the performances of current scheme for viscous flows [7]. In this case, an ideal gas is at rest in a two-dimensional unit box $[0, 1] \times [0, 1]$. A membrane located at $x = 0.5$ separates two different states of the gas and the dimensionless initial states are

$$(\rho, U, p) = \begin{cases} (120, 0, 120/\gamma), & 0 < x < 0.5, \\ (1.2, 0, 1.2/\gamma), & 0.5 < x < 1, \end{cases}$$

where $\gamma = 1.4$, Reynolds number Re $= 200$ and Prandtl number Pr $= 0.73$. In the computation, this case is tested in the physical domain $[0, 1] \times [0, 0.5]$, a symmetric boundary condition is used on the top boundary $x \in [0, 1]$, $y = 0.5$. Non-slip boundary condition for velocity, and adiabatic condition for temperature are imposed at solid wall boundaries. The membrane is removed at time zero and wave interaction occurs. A boundary layer is generated at the beginning, and a shock moves to the right followed by a contact discontinuity. After reflected by the end wall, the discontinuities interact with the boundary layer.
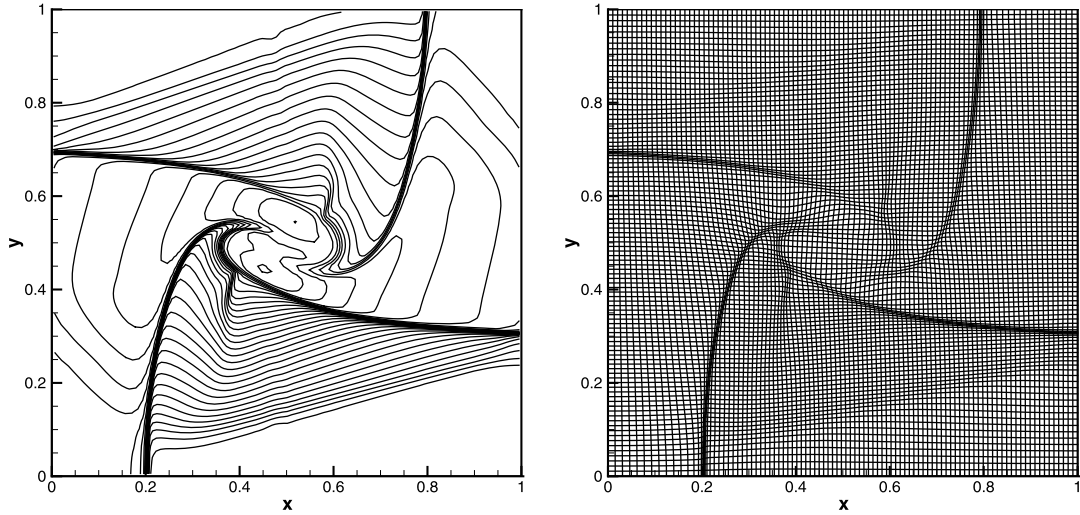
Fig. 14. Two dimensional Riemann problem: the density distribution (left) and mesh distribution (right) for four contact discontinuity interaction with 100×100 cells.
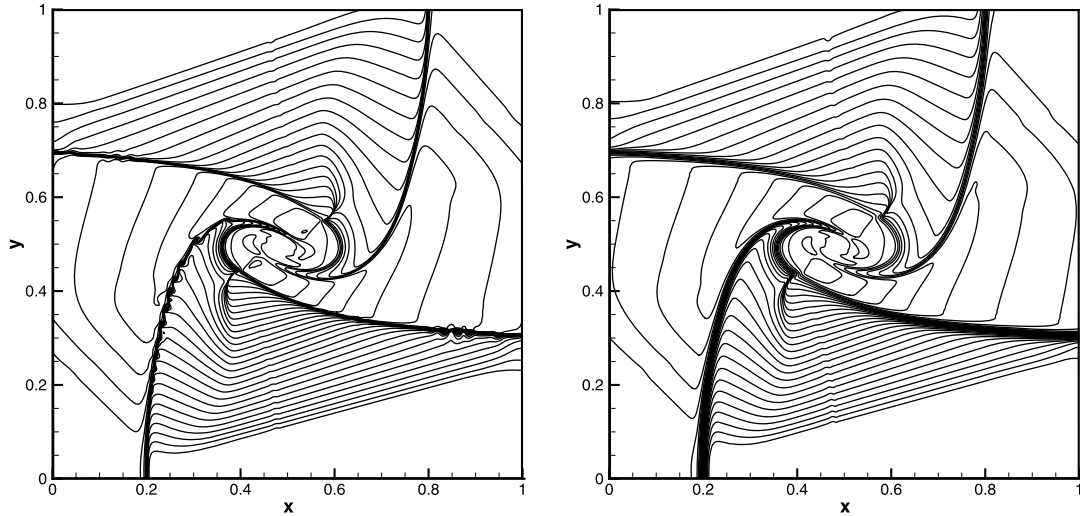

Fig. 15. Two dimensional Riemann problem: the density distribution on moving-mesh (left) and stationary mesh (right) for four contact discontinuity interaction with 400×400 cells.

Due to the inviscid and viscous coupling of gas-kinetic scheme, the current ALE method can be extended to computation for Navier-Stokes equations. To well resolve the complicated two-dimensional shock/shear/boundary-layer interactions, an anisotropy mesh needs to be generated during this procedure. Deferent monitor functions for x and y coordinates takes

$$\omega_x = \sqrt{1 + 0.0001 |\partial_x(\log \rho)|^2},$$

and

$$\omega_y = \sqrt{1 + 0.01 |\partial_y(\log \rho)|^2 + 0.01 |\partial_y \sqrt{U^2 + V^2}|}.$$

The computational mesh with 100×50 cells at $t = 0.25, 0.5, 0.75$ and 1 are given in Fig. 16 to present the adaptation procedure. The density distributions on the mesh with 500×250 and 700×350 cells are presented in Fig. 17 as well. As shown in Table 9, the height of primary vortex predicted by the current scheme agrees well with the reference data [18]. However, due to the nonlinear combination of linear polynomial, the current scheme is more dissipative than the fifth-order WENO reconstruction on structured meshes. Currently, the development of higher-order WENO on unstructured meshes is in progress.
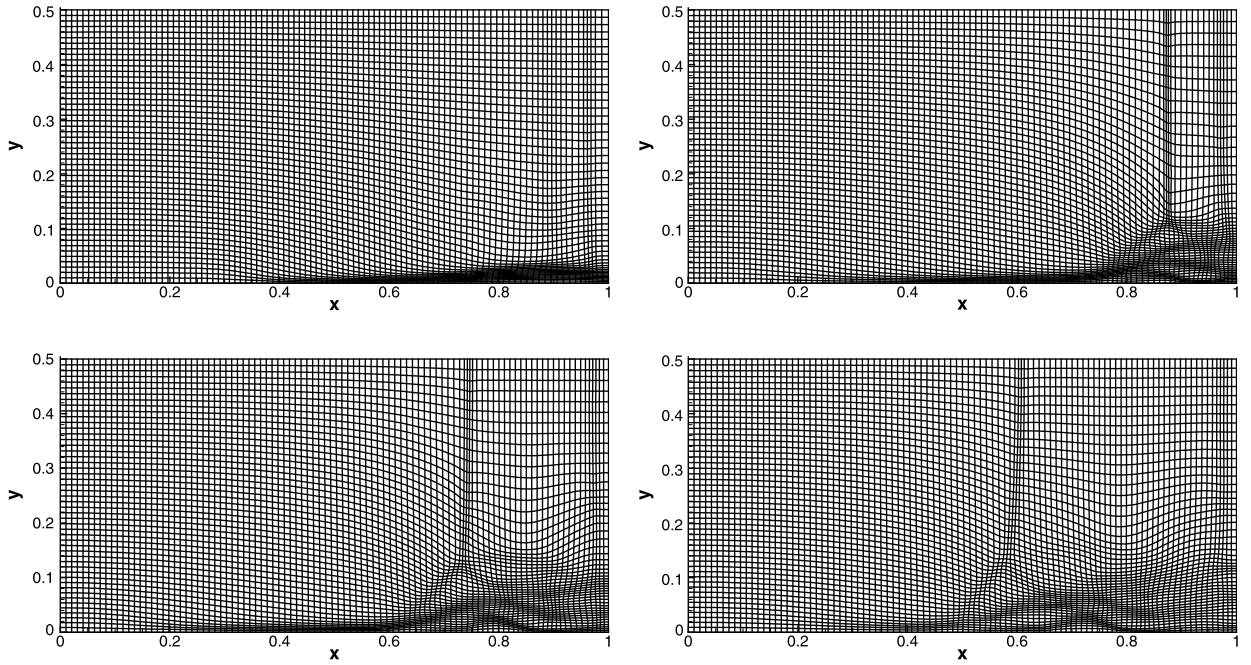
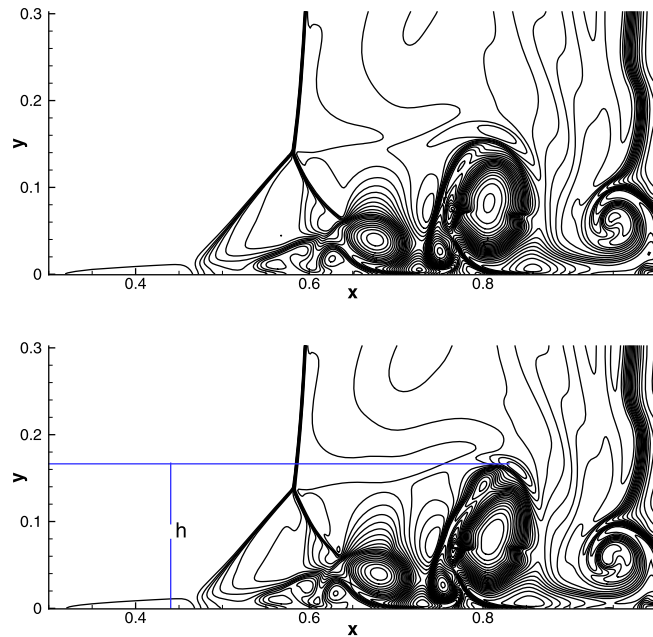**Fig. 16.** Viscous shock tube: the computational mesh at $t = 0.25, 0.5, 0.75$ and 1.

Fig. 17. Viscous shock tube: the density distributions on the mesh with 500×250 and 700×350 cells.

Table 9
Viscous shock tube: comparison of primary vortex heights among different schemes.

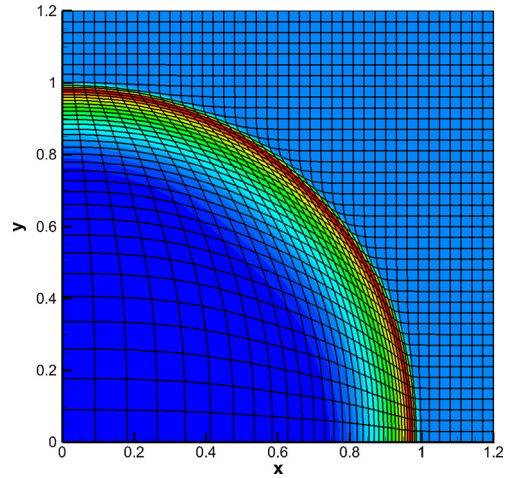| Scheme	AUSMPW+ [18]	M-AUSMPW+ [18]	WENO-GKS	GKS-ALE
Height	0.163	0.168	0.171	0.164

Fig. 18. Sedov problem: the mesh and density distribution at $t = 1$ with 40×40 cells.
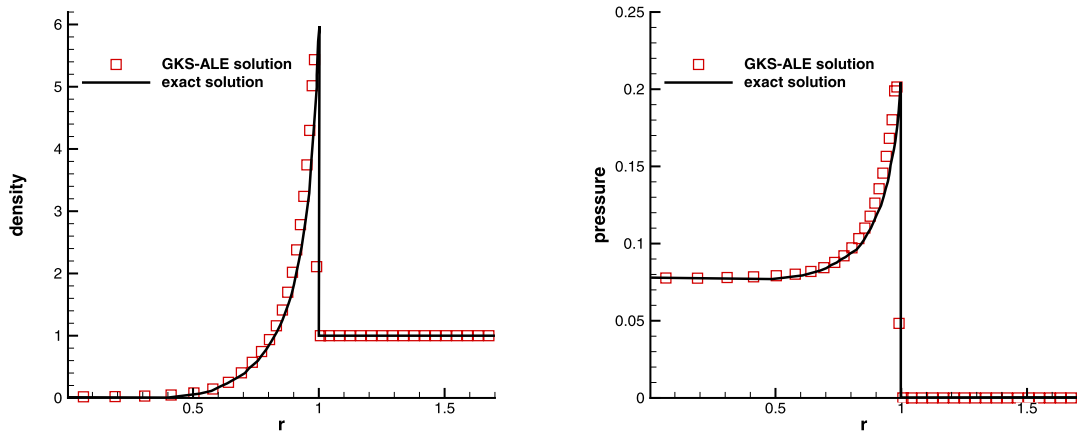
Fig. 19. Sedov problem: the density and pressure distribution along the diagonal line $t = 1$.

5.7. Sedov blast wave problem

This is a two-dimensional explosion problem to model blast wave from an energy deposited singular point, which is a standard benchmark problem for the Lagrangian method. The fluid is modeled by the ideal gas EOS with $\gamma = 1.4$. The initial density has a uniform unit distribution, and the pressure is 10^{-6} everywhere, except in the cell containing the origin. To run the case with smaller initial pressure, the positivity preserving technique may be considered in the future. For this cell containing the origin, the pressure is defined as $p = (\gamma - 1)\varepsilon_0/V$, where $\varepsilon_0 = 0.244816$ is the total amount of released energy and V is the cell volume. The reflection condition is used for the left and bottom boundaries, and non-reflection condition is used for the right and top boundaries. The computation domain is $[0, 1.2] \times [0, 1.2]$ and 40×40 cells are equally distributed initially. The density distribution at $t = 1$ is given in Fig. 18. The solution consists of a diverging infinite strength shock wave whose front is located at radius $r = 1$ at $t = 1$ [17]. The density and pressure profile along the diagonal line $t = 1$ are given in Fig. 19, and the numerical results agrees well with the exact solutions.

5.8. Saltzman problem

This is a benchmark test case for Lagrangian and ALE codes, which tests the ability to capture the shock propagation with a systematically distorted mesh [8,5]. The computational domain is $[0, 1] \times [0, 0.1]$. The initial mesh, which is given in Fig. 20, is expressed as

$$x_{ij} = i\Delta x + (10 - j)\Delta y \sin(\frac{i\pi}{100}),$$

$$y_{ij} = j\Delta y,$$

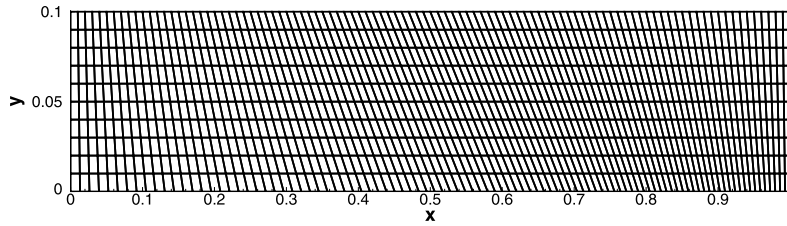**Fig. 20.** Saltzman problem: the initial mesh distribution.
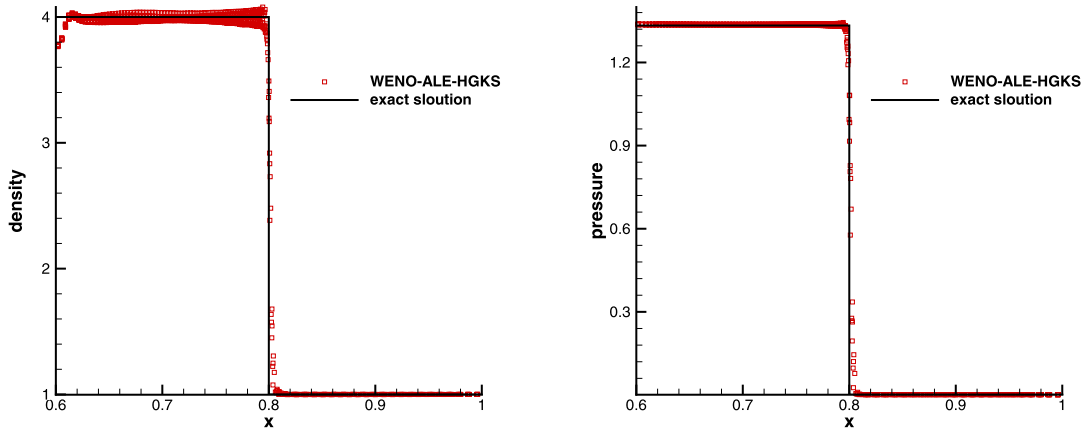

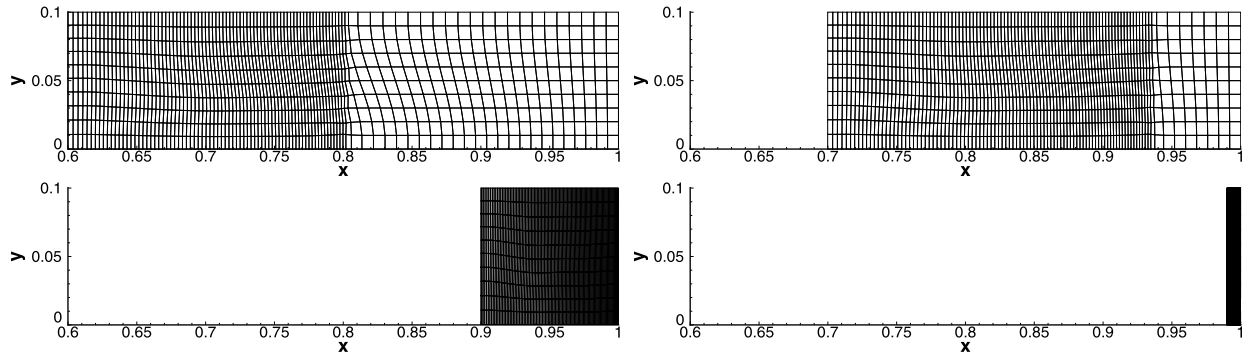**Fig. 21.** Saltzman problem: the density and pressure distribution in all the cells at $t = 0.6$.

Fig. 22. Saltzman problem: the mesh distribution at $t = 0.6, 0.75\ 0.9$ and 0.99.

where $\triangle x = \triangle y = 0.01$, and $i = 0, ..., 100, j = 0, ..., 10$. An ideal monatomic gas with $\rho = 1, e = 10^{-4}, \gamma = 5/3$ is filled in the box. The left-hand side wall acts as a piston with a constant velocity $U_p = 1$, and other boundaries are reflective walls. As a consequence, a strong shock wave is generated from the left end. For this case, the purely Lagrangian method will cause mesh deformation, and the ALE method works well because of the proper choice mesh velocity. At time $t = 0.6$, the shock is expected to be located at $x = 0.8$, and the post shock solutions are $p = 4$ and $p = 1.333$. The density and pressure distribution in all the cells is given in Fig. 21. The numerical results agrees well with the exact solutions. The shock wave will hit the face $x = 1$ at time $t = 0.75$ and be reflected by the solid wall. A second shock wave is produced which is traveling back towards the piston. Finally, the computation stops $t = 0.99$ because the shock wave generated by the wall collision matches the piston. The mesh distributions at $t = 0.6, 0.75\ 0.9$ and 0.99 are given in Fig. 22.

6. Conclusion

With the arbitrary Lagrangian-Eulerian (ALE) formulation, a high-order moving-mesh gas-kinetic scheme is presented for the inviscid and viscous flows. It extends the third-order gas kinetic method from a static domain to the flow simulation over a variable domain. In the moving-mesh procedure, the mesh becomes distorted, and a newly developed WENO reconstruction is used, in which the optimization approach for linear weights and the non-linear weights with new smooth indicator are proposed to improve the robustness of reconstruction. The two-stage fourth-order method is used for the

temporal discretization, and the second-order gas-kinetic solver is used for the flux calculation. In the two-stage method, the spatial reconstruction is performed at the initial and intermediate stages, while the computational meshes are given through a specified mesh velocity. To take the variation of mesh velocity along each cell interface into account, the WENO reconstruction is performed at each Gaussian quadrature point in the local moving coordinate. The analysis for geometric conservation law is also given. Numerical examples are presented to validate the performance of current scheme, where the mesh adaptation method and the cell centered Lagrangian method can be used to provide mesh velocity.

Declaration of competing interest

The authors declared that they have no known competing financial interests or personal relationships that could have appeared to influence the work reported in this paper.

Acknowledgements

References

[1] A.J. Barlow, P.H. Maire, W.J. Rider, R.N. Rieben, M.J. Shashkov, Arbitrary Lagrangian.Eulerian methods for modeling high-speed compressible multimaterial flows, J. Comput. Phys. 322 (2016) 603–665.
[2] M. Ben-Artzi, J. Li, Hyperbolic conservation laws: Riemann invariants and the generalized Riemann problem, Numer. Math. 106 (2007) 369–425.
[3] D.J. Benson, Computational methods in Lagrangian and Eulerian hydrocodes, Comput. Methods Appl. Mech. Eng. 99 (1992) 235–394.
[4] P.L. Bhatnagar, E.P. Gross, M. Krook, A model for collision processes in gases I: small amplitude processes in charged and neutral one-component systems, Phys. Rev. 94 (1954) 511–525.
[5] W. Boscheri, M. Dumbser, An efficient quadrature-free formulation for high order arbitrary-Lagrangian-Eulerian ADER-WENO finite volume schemes on unstructured meshes, J. Sci. Comput. 66 (2016) 240–274.
[6] S. Chapman, T.G. Cowling, The Mathematical Theory of Non-Uniform Gases, third edition, Cambridge University Press, 1990.
[7] V. Daru, C. Tenaud, Numerical simulation of the viscous shock tube problem by using a high resolution monotonicity-preserving scheme, Comput. Fluids 38 (2009) 664–676.
[8] J.K. Dukowicz, B. Meltz, Vorticity errors in multidimensional lagrangian codes, J. Comput. Phys. 99 (1992) 115–134.
[9] Z.F. Du, J.Q. Li, A Hermite WENO reconstruction for fourth order temporal accurate schemes based on the GRP solver for hyperbolic conservation laws, J. Comput. Phys. 355 (2018) 385–396.
[10] V. Dyadechko, M.J. Shashkov, Reconstruction of multi-material interfaces from moment data, J. Comput. Phys. 11 (2008) 5361–5384.
[11] S. Galera, P.H. Maire, J. Breil, A two-dimensional unstructured cell-centered multi-material ALE scheme using VOF interface reconstruction, J. Comput. Phys. 229 (2010) 5755–5787.
[12] W.H. Hui, P.Y. Li, Z.W. Li, A unified coordinated system for solving the two-dimensional Euler equations, J. Comput. Phys. 153 (1999) 596–637.
[13] C. Hu, C.W. Shu, Weighted essentially non-oscillatory schemes on triangular meshes, J. Comput. Phys. 150 (1999) 97–127.
[14] C.W. Hirt, A.A. Armsden, J.L. Cook, An arbitrary Lagrangian Eulerian computing method for all flow speed, J. Comput. Phys. 135 (1997) 203–216.
[15] C.Q. Jin, K. Xu, A unified moving grid gas-kinetic method in Eulerian space for viscous flow computation, J. Comput. Phys. 222 (2007) 155–175.
[16] C.Q. Jin, K. Xu, S.Z. Chen, A three dimensional gas-kinetic scheme with moving mesh for low-speed viscous flow computations, Adv. Appl. Math. Mech. 2 (2010) 746–762.
[17] J.R. Kamm, F.X. Timmes, On efficient generation of numerically robust Sedov solutions, Technical Report LA-UR-07-2849, Los Alamos National Laboratory, 2007.
[18] K.H. Kim, C. Kim, Accurate, efficient and monotonic numerical methods for multi-dimensional compressible flows Part I: Spatial discretization, J. Comput. Phys. 208 (2005) 527–569.
[19] M. Kucharik, R.V. Garimella, S.P. Schofield, M.J. Shashkov, A comparative study of interface reconstruction methods for multi-material ALE simulations, J. Comput. Phys. 229 (2010) 2432–2452.
[20] M. Kucharik, M. Shashkov, Conservative multi-material remap for staggered multi-material arbitrary Lagrangian-Eulerian methods, J. Comput. Phys. 258 (2014) 268–304.
[21] P.D. Lax, X.D. Liu, Solution of two-dimensional Riemann problems of gas dynamics by positive schemes, SIAM J. Sci. Comput. 19 (1998) 319–340.
[22] J. Li, Q. Li, K. Xu, Comparison of the generalized Riemann solver and the gas-kinetic scheme for inviscid compressible flow simulations, J. Comput. Phys. 230 (2011) 5080–5099.
[23] J.Q. Li, Z.F. Du, A two-stage fourth order time-accurate discretization for Lax-Wendroff type flow solvers I. hyperbolic conservation laws, SIAM J. Sci. Comput. 38 (2016) 3046–3069.
[24] P.H. Maire, R. Abgrall, J. Breil, J. Ovadia, A cell-centered Lagrangian scheme for two-dimensional compressible flow problems, SIAM J. Sci. Comput. 29 (2007) 1781–1824.
[25] V.T. Nguyen, An arbitrary Lagrangian-Eulerian discontinuous Galerkin method for simulations of flows over variable geometries, J. Fluids Struct. 26 (2010) 312–329.
[26] G.X. Ni, S. Jiang, K. Xu, Remapping-free ALE-type kinetic method for flow computations, J. Comput. Phys. 228 (2009) 3154–3171.
[27] L. Pan, K. Xu, Q.B. Li, J.Q. Li, An efficient and accurate two-stage fourth-order gas-kinetic scheme for the Navier-Stokes equations, J. Comput. Phys. 326 (2016) 197–221.
[28] L. Pan, J.Q. Li, K. Xu, A few benchmark test cases for higher-order Euler solvers, Numer. Math., Theory Methods Appl. 10 (2017) 711–736.
[29] L. Pan, K. Xu, Two-stage fourth-order gas-kinetic scheme for three-dimensional Euler and Navier-Stokes solutions, Int. J. Comput. Fluid Dyn. 32 (2018) 395–411.
[30] L. Pan, K. Xu, High-order gas-kinetic scheme with three-dimensional WENO reconstruction for the Euler and Navier-Stokes solutions, arXiv:1909.01580v1.

[31] P.O. Persson, J. Bonet, J. Peraire, Discontinuous Galerkin solution of the Navier-Stokes equations on deformable domains, Comput. Methods Appl. Mech. Eng. 198 (2009) 1585–1595.
[32] X.D. Ren, K. Xu, W. Shyy, A multi-dimensional high-order DG-ALE method based on gas-kinetic theory with application to oscillating bodies, J. Comput. Phys. 316 (2016) 700–720.
[33] J. Shi, C. Hu, C.W. Shu, A technique of treating negative weights in WENO schemes, J. Comput. Phys. 175 (2002) 108–127.
[34] H.Z. Tang, T. Tang, Adaptive mesh methods for one-and two-dimensional hyperbolic conservation laws, SIAM J. Numer. Anal. 41 (2003) 487–515.
[35] P. Thomas, C. Lombard, Geometric conservation law and its application to flow computations on moving grids, AIAA J. 17 (1979) 1030–1037.
[36] E.F. Toro, Riemann Solvers and Numerical Methods for Fluid Dynamics, third edition, Springer, 2009.
[37] P. Vachal, R.V. Garimella, M.J. Shashkov, Untangling of 2D meshes in ALE simulations, J. Comput. Phys. 196 (2004) 627–644.
[38] K. Xu, Direct Modeling for Computational Fluid Dynamics: Construction and Application of Unfied Gas Kinetic Schemes, World Scientific, 2015.
[39] K. Xu, A gas-kinetic BGK scheme for the Navier-Stokes equations and its connection with artificial dissipation and Godunov method, J. Comput. Phys. 171 (2001) 289–335.
[40] F.X. Zhao, L. Pan, S.H. Wang, Weighted essentially non-oscillatory scheme on unstructured quadrilateral and triangular meshes for hyperbolic conservation laws, J. Comput. Phys. 374 (2018) 605–624.